PAPER

Electrical and thermoelectric properties of a poly(3-(2-octyldodecyl)thiophene)/poly(3-octylthiophene)/2,3,5,6-tetrafluoro-7,7',8,8'-tetracyanoquinodimethane viscoelastic polymer blend doping system

Roujun Chen,†[a,b] Zijian Yin,†[a] Zhongming Chen ORCID *[c] and Chengjun Pan ORCID *[a]

Organic thermoelectric materials have attracted significant research interest due to their unique advantages. Chemical doping serves as a key strategy for enhancing the thermoelectric performance of conductive polymers by modulating their electronic structures and physical properties. In this study, we investigated the electrical and thermoelectric properties of blend-doped composites comprising poly(3-(2-octyldodecyl)thiophene) (P3ODT, with branched alkyl side chains) and poly(3-octylthiophene) (P3OT, with linear alkyl side chains), doped with 2,3,5,6-tetrafluoro-7,7',8,8'-tetracyanoquinodimethane (F$_4$-TCNQ). The results demonstrated that incorporating P3ODT enhanced the flexibility and surface quality of the material. As the proportion of P3ODT increased in the test groups, the number of conductive complexes decreased, leading to a reduction in electrical conductivity. But the Seebeck coefficient of the blend-doped material initially rose continuously, reaching a maximum of 62.67 μV K^{-1} due to optimized carrier energy filtering, while it declined when the P3ODT : P3OT ratio reached 4 : 6. Notably, despite the lower conductivity, the thermoelectric performance peaked at a P3ODT : P3OT ratio of 1 : 9, achieving a power factor (PF) of 0.69 μW m^{-1} K^{-2}. Regarding the doping mechanism, F$_4$-TCNQ effectively induced the aggregation of P3OT and the generation of polarons/bipolarons. However, its doping reaction with P3ODT was limited, likely due to the steric hindrance caused by the bulky alkyl side chains of P3ODT. Nevertheless, the alkyl side chains enhanced carrier mobility through backbone planarization which compensated for the reduced carrier concentration and conductivity. These findings suggested that blending P3ODT as a second conjugated polymer with tailored side chains can offer an effective strategy to improve the thermoelectric properties of flexible organic materials, providing valuable molecular design principles for performance optimization.

Introduction

Thermoelectric (TE) materials are recognized for their ability to directly convert thermal energy, such as solar energy and waste heat, into electrical energy, making them a sustainable and strategically important class of materials.[1] While in-

[a] College of Materials Science and Engineering, State Key Laboratory of Fine Chemicals, Shenzhen University, Shenzhen 518060, P. R. China.
E-mail: pancj@szu.edu.cn
[b] Key Laboratory of Resources Environmental and Green Low Carbon Processes in East Guangdong, School of Chemistry and Environmental Engineering, Hanshan Normal University, Chaozhou, 521041, China
[c] School of Environment and Civil Engineering, Dongguan University of Technology, Dongguan 523808, China
† These authors contributed equally to this work.

organic TE materials exhibit excellent thermoelectric properties and high conversion efficiencies,[2,3] their applications are constrained by several drawbacks, including toxicity, high production costs, and mechanical brittleness. To address these challenges, flexible TE materials have gained prominence as promising alternatives, offering advantages such as abundant raw materials, lightweight design, mechanical flexibility, solution processability, and low-cost fabrication.[4,5] Among these, conjugated polymers, a key subset of flexible TE materials, are characterized by conjugated repeating units with alternating single and double bonds.[6] This structural feature allows π-electron delocalization along the polymer backbone, creating extended electron distribution pathways and intrinsic electrical conductivity.[7,8] Representative examples include polypyrroles,[9] polyanilines,[10] polyfluorenes, polyindoles, and polythiophenes.[11,12] Crucially, the reversible doping behavior

© 2025 The Author(s). Published by the Royal Society of Chemistry

RSC Appl. Polym., 2025, **3**, 1629–1636 | **1629**

and doping range of these polymers significantly enhance the charge conductivity along the polymer backbone, which is a key factor in their preference for thermoelectric applications.

The solubility of conjugated polymers is governed by their side-chain architecture, particularly the size and the length of alkyl side chains, which critically influence material properties and device performance.[13–15] These polymers are categorized as viscoelastic conjugated polymers (VE-CPs), characterized by a rigid π-conjugated backbone paired with flexible side-chain structures. The side chains act as "internal plasticizers", balancing mechanical flexibility with electronic functionality. To systematically tune these properties, researchers have employed side-chain engineering strategies. For instance, Pan et al.[16] modulated the alkyl-to-π ratio in polyfluorene derivatives via "alkyl-π" engineering, enabling precise control over the polymer phase behavior—transitioning from a fluid to a viscoelastic and ultimately solid state. Similarly, Shinohara et al.[17] designed poly(phenylene-benzothiadiazolyl-bis(thiophene)) as the backbone and elongated its dendrimer-like alkyl side chains. This modification improved the polymer's mechanical stability at room temperature, inducing a solvent-free transition from a brittle glassy state to a viscoelastic state without compromising its fluorescence properties. Collectively, these studies demonstrate that branching alkyl side chains on π-conjugated backbones (e.g., in poly(thiophene)) enhance the mechanical robustness of VE-CPs, a critical advancement for developing durable, high-performance organic thermoelectric materials.

The thermoelectric properties of materials are typically quantified by the power factor (PF = $S^2\sigma$), where S is the Seebeck coefficient and σ is the electrical conductivity. At a fixed temperature, both S and σ depend on the energy difference between the Fermi energy (E_F) and the transport energy (E_{tr}), expressed as $S \propto (E_F - E_{tr})/T$ and $\sigma \propto \exp[(E_F - E_{tr})/T]$. Here, E_F is modulated by carrier concentration and electronic states, while E_{tr} corresponds to the energy range within the density of states (DOS) that contributes to charge transport. To optimize the PF, researchers employ chemical doping to adjust E_F by increasing the intrinsic carrier concentration, thereby balancing S and σ.[18,19] For example, Chabinyc et al.[20] systematically studied the doping effects of fluoroalkyltrichlorosilanes (FTS) and 2,3,5,6-tetrafluoro-7,7′,8,8′-tetracyanoquinodimethane (F$_4$-TCNQ) on poly(3-hexylthiophene) (P3HT) and poly[2,5-bis(3-tetradecylthiophen-2-yl)thieno[3,2-b]thiophene] (PBTTT-C14). Their work demonstrated that optimizing dopant selection enhances the electrical conductivity and PF by up to 200-fold and 20-fold, respectively, in these polythiophene derivatives.

F$_4$-TCNQ is particularly effective due to its ability to induce ground-state charge transfer with conjugated polymers, generating polarons and bipolarons that improve charge transport. For instance, in doped P3HT, electrons transfer from the polymer's highest occupied molecular orbital (HOMO) to the dopant's lowest unoccupied molecular orbital (LUMO), achieving integer charge transfer.[21,22] Building on this, David Kiefer et al.[23] reported that double doping with F$_4$-TCNQ produces a high doping efficiency of 170% at low concentrations, as a large fraction of generated carriers participate in conduction. These findings highlight F$_4$-TCNQ and its derivatives as versatile dopants for conjugated polymers, enabling efficient charge modulation at minimal doping levels—a critical strategy for advanced organic thermoelectrics.

The ionization of dopants can significantly alter the DOS within conjugated polymers, which plays a pivotal role in the charge and energy transport properties of organic TE materials. However, at high doping concentrations, this process often induces a disordered surface morphology in doped polymers, which degrades charge transport pathways and ultimately limits TE performance optimization.[24,25] To resolve this trade-off between the doping level and morphology, researchers have developed polymer blending strategies that synergize complementary properties of distinct conjugated polymers. For instance, Martens[26] proposed a theoretical framework for blend systems composed of two polymers with differing energy landscapes. Their model incorporates a triangular transport distribution above the E_F, demonstrating that such blends enhance charge transport by creating two distinct DOS profiles. Experimentally, Zuo et al.[27] validated this concept by fabricating binary blends of conjugated polymers with mismatched HOMO energy levels. By adjusting the blend ratio, they observed a systematic shift in the E_{tr} toward the DOS of the dominant polymer. This approach enables precise control over the Seebeck coefficient while maintaining high electrical conductivity, thereby optimizing the PF and advancing TE performance in blended systems.

Organic thermoelectric materials offer compelling advantages over inorganic counterparts, including resource sustainability, mechanical flexibility, solution processability, and low-cost fabrication. The TE performance of conjugated polymers can be optimized by enhancing electrical conductivity through chemical doping, with the carrier concentration being highly dependent on the doping efficiency. Thus, strategic selection of dopant type and concentration is significant for maximizing TE properties. Building on this principle, we employed a viscoelastic conjugated polymer with nonpolar 3-(2-octyldodecyl) thiophene side chains using an "alkyl-π" engineering strategy. This polymer was blended with poly(3-octylthiophene) (P3OT) at varying weight ratios and molecularly doped with F$_4$-TCNQ to systematically investigate TE performance trends in the blended systems. This study aims to elucidate the response of the novel blended polymers to chemical doping and to provide a theoretical basis for the optimization of future thermoelectric material performance.

Experimental section

Materials

Sodium thiosulfate (Na$_2$S$_2$O$_3$, 98%) and [1,3-bis(diphenylphosphino)propane]nickel(II) chloride (Ni(dppp)Cl$_2$, C$_{27}$H$_{26}$Cl$_2$NiP$_2$, 98%) were purchased from Anhui Zesheng Technology Co., Ltd. N-Bromosuccinimide (NBS, C$_4$H$_4$BrNO$_2$, 98%), isopropyl-

magnesium chloride (iPr-MgCl, C_3H_7ClMg, 98%), and 2,3,5,6-tetrafluoro-7,7′,8,8′-tetracyanoquinodimethane (F_4-TCNQ, $C_{12}F_4N_4$, 97%) were obtained from Shanghai Macklin Biochemical Co., Ltd. Chloroform ($CHCl_3$, A.R.) and hydrochloric acid (HCl, C.R.) were sourced from Sinopharm Chemical Reagent Co., Ltd and Damao Chemical Reagent Factory, respectively. All solvents, including anhydrous-grade reagents, were supplied by Anhui Zesheng Technology Co., Ltd.

Synthesis

2,5-Dibromo-3-octylthiophene (S1) and 2,5-dibromo-3-(2-octyldodecyl)thiophene (S2). In a double-necked flask (Flask A), 3-octylthiophene (1.5 g, 1.0 eq.) was dissolved in anhydrous THF (20 mL) under a nitrogen atmosphere. Concurrently, N-bromosuccinimide (NBS, 2.07 g, 2.1 eq.) was dissolved in anhydrous THF (30 mL) in a separate double-necked flask (Flask B). The NBS solution was then slowly added to Flask A via a syringe under an ice-water bath, and the reaction mixture was stirred at 0 °C for 30 minutes. After removing the ice bath, the reaction was allowed to proceed at room temperature in the absence of light for 6 hours. Upon completion, the mixture was extracted with n-hexane and washed with a 10% aqueous sodium thiosulfate solution. The organic layer was dried over anhydrous $MgSO_4$, filtered, and concentrated by rotary evaporation to afford the crude product. Purification via column chromatography (n-hexane as an eluent) yielded S1 as a colorless transparent-oily product with an 87% yield. For the synthesis of S2, an identical procedure was employed using 3-(2-octyldodecyl)thiophene (2 g, 1.0 eq.) and NBS (2.15 g, 2.2 eq.), yielding S2 as a colorless transparent-oily product in 84% yield.

Poly(3-alkylthiophene) (P3ODT, P3OT) with different alkyl side chains. Poly(3-alkylthiophenes) were synthesized via catalyst transfer polycondensation (CTP), with S1 and S2 employed in a catalyst ratio of 100:1 and 150:1, respectively, for the preparation of poly(3-octylthiophene) (P3OT) and poly(3-(2-octyldodecyl)thiophene) (P3ODT). The synthesis procedure for P3ODT is detailed below as a representative example:

Under a nitrogen atmosphere, S2 (500 mg, 1 eq.) was vacuum-dried at 60 °C for 4 h to remove residual moisture. The dried monomer was then dissolved in anhydrous THF (10 mL) in a double-necked flask (Flask C), and the solution was degassed via vacuum heating at 40 °C for 10 min with vigorous stirring. Flask C was cooled to 0 °C in an ice-water bath, and i-PrMgCl (0.95 mmol, 0.98 eq.) was added dropwise via a syringe. The reaction mixture was shielded from light with aluminum foil and stirred at room temperature for 30 min to ensure complete monomer activation. In parallel, the catalyst Ni(dppp)Cl_2 (0.0128 mmol, 0.0067 eq.) was loaded into a double-necked flask (Flask D) under nitrogen and suspended in anhydrous THF (2 mL). This catalyst suspension was then slowly injected into Flask C, triggering an immediate color change to orange-red accompanied by bright orange-red fluorescence under UV light (365 nm), indicative of polymer chain propagation. The reaction was maintained at 45 °C for 12 h under continuous stirring. After being cooled to room temperature, the polymerization was quenched by adding 1 M HCl

(5 mL). The crude product was extracted by partitioning the mixture between deionized water (20 mL) and chloroform (30 mL). The organic layer was isolated, dried over anhydrous $MgSO_4$, filtered, and concentrated via rotary evaporation. The resulting residue was dissolved in chloroform (5 mL) and precipitated into methanol (50 mL) in a centrifuge tube. The suspension was centrifuged at 6000 rpm for 10 min, and the supernatant was decanted to remove unreacted monomers and oligomers. This precipitation–centrifugation cycle was repeated three times. The final polymer-rich precipitate was vacuum-dried at 40 °C for 12 h, yielding 320 mg (66%) of P3ODT as a viscous orange-red solid.

Preparation of P3ODT/P3OT/F_4-TCNQ viscoelastic polymer blend solutions and films. P3ODT/P3OT blend solutions were prepared by mixing the two polymers in mass ratios of 0:10, 1:9, 2:8, 3:7, and 4:6 (P3ODT:P3OT). Each mixture was dissolved in anhydrous o-dichlorobenzene (ODCB) at a concentration of 5 mg mL^{-1} and stirred at 60 for 2 h to ensure complete dissolution, resulting in a homogeneous orange-red solution. Separately, F_4-TCNQ was dissolved in chloroform at a concentration of 1 mg ml^{-1}. Chloroform was selected as the dopant solvent due to its lower boiling point (61 °C) compared to ODCB (180 °C), enabling precise control over solvent evaporation during film formation to minimize defects.

Then 1 mL of each of the P3ODT/P3OT (0:10, 1:9, 2:8, 3:7, 4:6) blend solutions was combined with the F_4-TCNQ solution, achieving doping levels of F_4-TCNQ of 20 wt%, 18 wt%, 16 wt%, 14 wt%, and 12 wt%, respectively. Additional chloroform was added to standardize the volume of each of the blend solutions. These doped blend solutions were sonicated for 1 h to ensure uniform dispersion of F_4-TCNQ and molecular-level doping of the polymer matrix. The 20 wt% doping level was selected based on prior optimization studies, which indicate that this concentration maximizes charge-transfer efficiency between F_4-TCNQ and P3OT while avoiding phase separation. Finally, 100 μL of each of the doped blend solutions were carefully drop-cast onto 1 cm × 1 cm glass substrates using a pipette. The films were dried under ambient conditions (25 °C, 45% relative humidity) in a dark environment for 24 h to prevent photo-oxidation and ensure controlled solvent evaporation. This process yielded flexible P3ODT/P3OT/F_4-TCNQ blend films with varying mass ratios.

Results and discussion

Characterization of synthetic polymers

In this study, monomers S1 and S2 were synthesized via bromination, followed by the preparation of P3OT and P3ODT through catalyst-transfer polycondensation. The structures of these polymers were confirmed by ^{1}H NMR spectroscopy (Fig. S1–S4), while their molecular weights and dispersity were determined via gel permeation chromatography (Fig. S5 and Table S1). Both polymers exhibited molecular weights consistent with synthetic targets, with closely matched values between P3OT and P3ODT. TGA confirmed the excellent

© 2025 The Author(s). Published by the Royal Society of Chemistry

RSC Appl. Polym., 2025, **3**, 1629–1636 | **1631**

thermal stability of P3OT and P3ODT with 5% weight loss up to 409 °C and 424 °C, well beyond our measurement range. FTIR analysis (Fig. 1A) revealed a distinct cyanide band at ~2225 cm^{-1} for pure F$_4$-TCNQ. In contrast, the undoped polymers exhibited no discernible absorption peak in this region. After doping, the blended P3OT/F$_4$-TCNQ system displayed a redshifted absorption peak at ~2191 cm^{-1} ($\Delta\nu \approx 34$ cm^{-1}, Fig. 1B), indicative of integer charge transfer between P3OT and F$_4$-TCNQ, consistent with the formation of F$_4$-TCNQ^{-1} species.[22,28,29] Conversely, doped P3ODT exhibited a significantly smaller shift ($\Delta\nu \approx 17$ cm^{-1}), approximately half the magnitude observed for P3OT, suggesting partial charge transfer involving electron sharing across multiple sites. This distinction implies complete doping in P3OT but incomplete doping in P3ODT under these conditions. Furthermore, the absence of residual peaks at 2225 cm^{-1} after doping indicates full participation of F$_4$-TCNQ in both systems, although with differing charge-transfer efficiencies.

XRD spectroscopy

The crystalline structures of P3OT, P3ODT and their doped blends were analyzed *via* X-ray diffraction (XRD, Fig. 2). As shown in Fig. 2A, P3OT displayed sharp diffraction peaks at 4.2°, 8.5°, 12.9° and 23.4°, as well as a broad diffuse peak at 18.4°, confirming its crystalline nature. In contrast, P3ODT exhibited no distinct diffraction peaks but a prominent diffuse halo at 20°, indicative of an amorphous structure lacking long-range order. This disparity may be attributed to the long-branched side chain of P3ODT, restricting close backbone stacking. For blended polymers (Fig. 2B), the (100) peak position remained unaltered, but its intensity decreased, reflecting reduced crystallinity due to blending. After doping, the (100) peak of P3OT shifted by 3.8° (from 4.2° to lower angles, Fig. 2C and Table S2), accompanied by an increase in interplanar spacing from 2.043 nm to 2.298 nm. This lattice expansion and peak broadening suggest doping-induced disordering, likely resulting from the destabilization of polaritons and lattice distortion. As the proportion of the blending phase P3ODT increased, the (100) peak broadened and the grain size decreased, reaching a minimum of 4.450 nm at a 3 : 7 P3ODT : P3OT ratio (Fig. 2C). These trends indicated that the interaction between P3ODT and P3OT lowered the crystallinity of the material to some extent. Compared to doped P3OT without blending, the doped P3ODT : P3OT material possessed a larger layer spacing, implying that the incorporation of P3ODT hindered the interlayer stacking of the polymers, resulting in some phase separation.

UV-vis-NIR spectroscopy

The structural and electronic changes in P3OT/P3ODT/F$_4$-TCNQ films were probed using UV-vis-NIR spectroscopy. Raman data (Fig. S7) revealed a broadening of the Cα = Cβ stretching vibrational peak to 1448.22 cm^{-1}, indicative of a shift in the film structure toward a more disordered state.
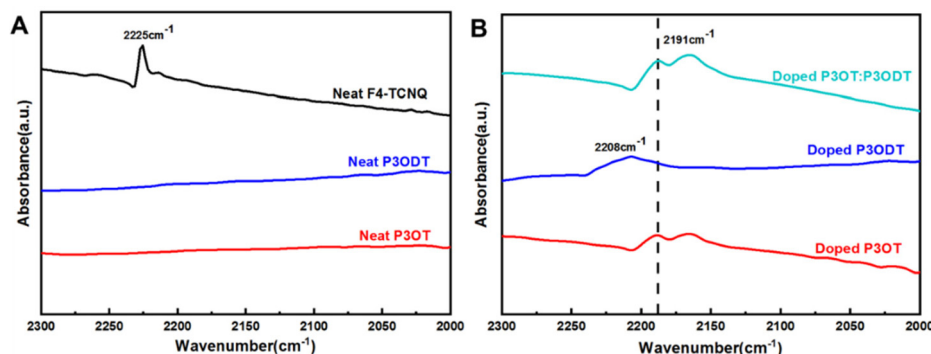

Fig. 1 (A) Infrared spectra of P3OT, P3ODT, and F$_4$-TCNQ. (B) Infrared spectra of P3OT, P3ODT, and P3ODT/P3OT blends in the doped state.
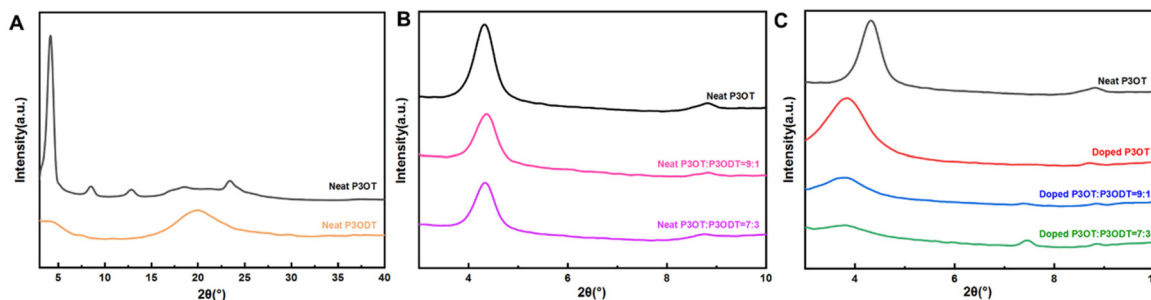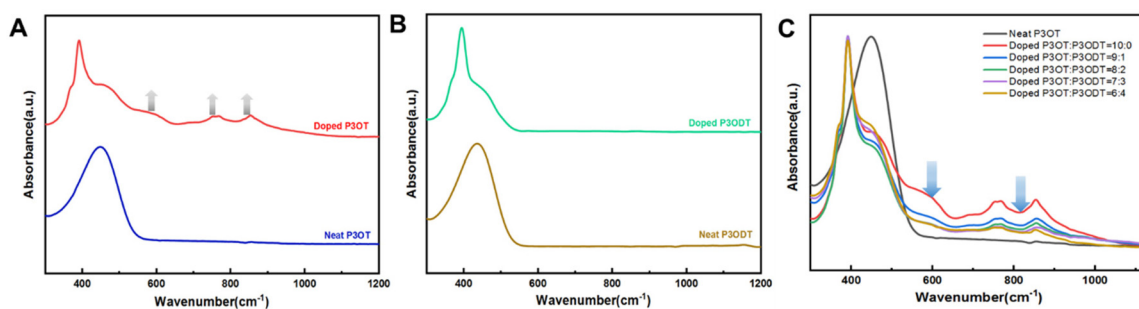

Fig. 2 (A) XRD diffraction patterns of P3OT and P3ODT. (B) XRD diffraction patterns of different blending ratio polymers. (C) XRD diffraction patterns of polymer/F4-TCNQ doped materials with varying blending ratios.

Fig. 3 (A) UV-vis-NIR spectra of the intrinsic and doping states of P3OT. (B) UV-vis-NIR spectra of intrinsic and doping states of P3ODT. (C) UV-vis-NIR spectra of P3ODT/P3OT doped states at different blending ratios.

Increasing the P3OT/P3ODT ratio induced a progressive red-shift in these peaks, consistent with a transition from a benzenoid to quinoid backbone conformation,[30,31] implying the formation of bipolarons. UV-vis-NIR analysis further elucidated this doping effect. As illustrated in Fig. 3A, the undoped P3OT showed a π–π* transition peak in the solvation state (s-P3OT) at approximately 450 nm, while a novel aggregation state absorption peak (nw-P3OT) emerged at 584 nm following doping, indicating that F_4-TCNQ promoted the polymer chain planarization. The sharp absorption peak at 391 nm was the F_4-TCNQ$^-$ produced after accepting electrons.[32] The reduction in the absorption peak of doped P3OT at ~450 nm was likely due to the electron transfer from the ground state of P3OT to F_4-TCNQ. This process diminished the internal electron density within P3OT, which in turn directly reflected the significant impact of the dopant F_4-TCNQ on the electronic structure of P3OT.[33,34] The absorption peaks at ~766 nm and ~855 nm implied the formation of polarons/bipolarons in the doped P3OT, which aligned with the results shown by Raman spectroscopy, confirming charge carrier generation.

In contrast, doped P3ODT (Fig. 3B) retained its intrinsic π–π* transition absorption peaks at 435 nm. Combined with Fig. 1B, although the doped P3ODT exhibited an electron-transfer shoulder and an F_4-TCNQ$^-$ absorption peak, the P3ODT$^+$ polariton resulting from the partial charge-transfer mechanism was not formed. This incomplete doping interaction was directly attributed to the steric hindrance imposed by the bulky size of the alkane-branched chain of P3ODT, which hindered interaction with the F_4-TCNQ, resulting in the formation of aggregates being prevented. Further supporting the limited interaction between P3ODT and F_4-TCNQ, Fig. 3C shows that the polaron/bipolaron peaks of P3OT declined with the increase of P3ODT content, which suggested that P3ODT impeded the interaction between P3OT and F_4-TCNQ, leading to a reduction in the carrier concentration. This phenomenon was likely due to the viscoelastic P3ODT, which might have wrapped around P3OT, hindering the reaction with F_4-TCNQ.

Microscopic morphology studies

The surface morphologies of P3OT films and P3ODT/P3OT blend films were examined using scanning electron microscopy (SEM) and atomic force microscopy (AFM). The results (Fig. 4A) showed that the surface of pure P3OT films was smooth and uniform without significant aggregation. However, with the increase of P3ODT content (Fig. 4B and C), the surface of the blended film became rough, and aggregation occurred. When the ratio of P3ODT/P3OT reached 3 : 7, island-like structures and voids emerged, which could be attributed to the poor mixing of P3OT and P3ODT in the solvent-free state, leading to phase separation and film deterioration. The introduction of the molecular dopant F_4-TCNQ led to the formation of particles on the unblended P3OT film (Fig. 4D), thus indicating the creation of conductive complexes between P3OT and F_4-TCNQ. Notably, as the proportion of P3ODT rose, higher P3ODT ratios in the blended systems suppressed the particle density (Fig. 4E and F), signifying a reduction in the number of conductive complexes. As shown in Fig. 4G, island-like structures could be observed in pure P3OT films *via* AFM, while such structures were absent in SEM images. After doping, the island structures diminished, while the number of conductive complexes increased, thereby enhancing the grain boundary density of the doped film[16] (Fig. 4H–J). Conversely, P3ODT-blended films lacked such islands and exhibited lower particle concentrations, consistent with SEM observations. In summary, the interaction of P3ODT/P3OT with F_4-TCNQ enhanced the film quality, whereas the blend of F_4-TCNQ with P3ODT improved the carrier mobility.

Thermoelectric properties

Fig. 5 shows that the thermoelectric properties of the P3ODT/P3OT/F_4-TCNQ viscoelastic polymer blended films depended on the blend ratio at room temperature. All blends displayed positive Seebeck coefficients, confirming p-type (hole-dominated) charge transport. At the blending ratio of 3 : 7, the Seebeck coefficients reached a maximum value of 62.67 μV K^{-1}. This was attributed to the incorporation of the second phase (P3ODT), which improved the material carrier mobility while optimizing the surface morphology of the film. However, the further increase in the P3ODT ratio instead made the Seebeck coefficients decrease, probably due to the large degree of separation of the two phases, resulting in the blockage of carrier mobility. The conductivity of the P3ODT/P3OT/F_4-TCNQ blend films exhibited a declining trend with the increase in the P3ODT ratio. This phenomenon was explained

© 2025 The Author(s). Published by the Royal Society of Chemistry

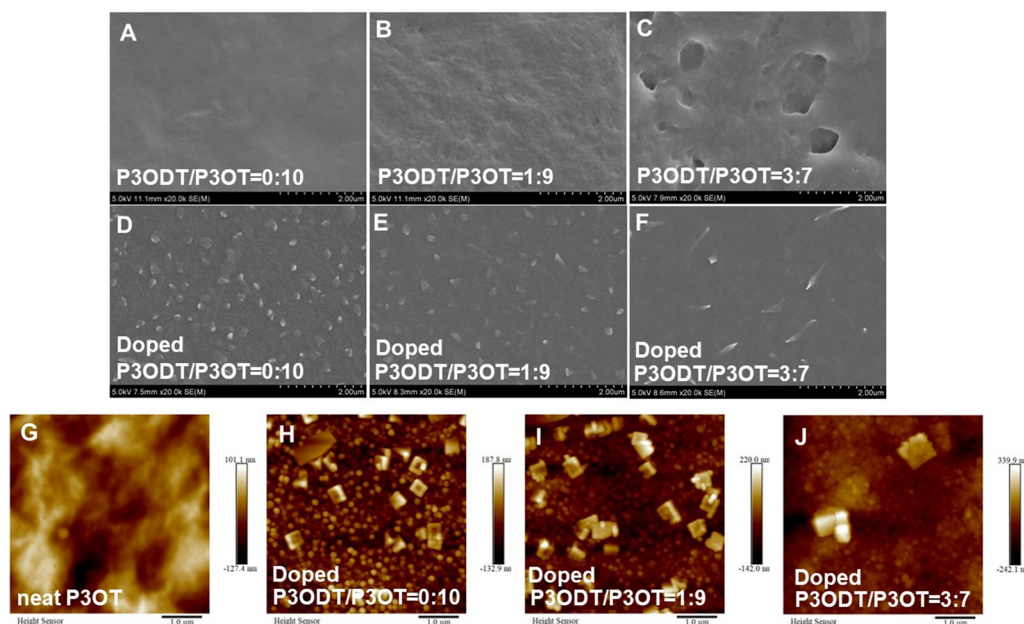*RSC Appl. Polym.*, 2025, **3**, 1629–1636 | **1633**

Fig. 4 (A–C) SEM images of different ratios of blending films. (D–F) SEM images of different ratios of blend-doped films. (G) AFM image of a neat P3OT film. (H–J) AFM images of different ratios of blend-doped films.
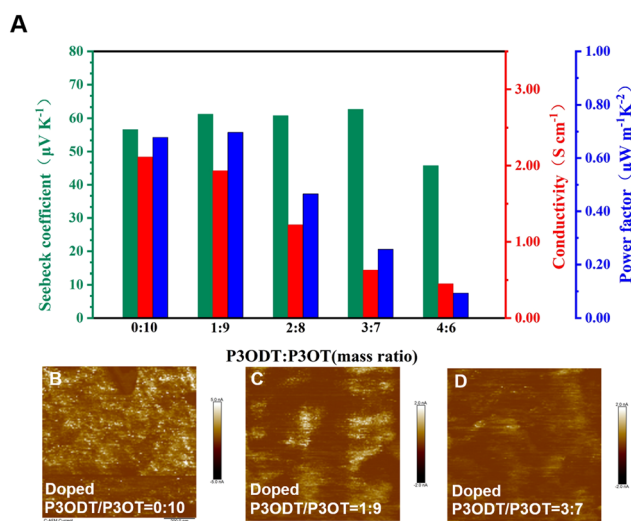

Fig. 5 (A) Thermoelectric properties of P3ODT/P3OT/F4-TCNQ films with different blending ratios. (B–D) C-AFM images of P3ODT/P3OT/F4-TCNQ films with different blending ratios.

by the inhibitory effect of P3ODT on the formation of conductive complexes, consequently reducing the carrier concentration of the films. The power factor (PF) reached its maximum value (0.697 μW m^{-1} K^{-2}) at a 1 : 9 P3ODT : P3OT ratio, indicating that although the P3ODT phase lowered the carrier concentration, the increase in carrier mobility could compensate for this decrease so that the PF value appeared ascending tendency. This also revealed that the introduction of another conjugated polymer into the conjugated polymer matrix in an appropriate amount would enhance the thermo-

electric properties of the blend materials. Conductive atomic force microscopy (C-AFM) corroborated these trends (Fig. 5B–D). Films with a 1 : 9 P3ODT : P3OT ratio showed optimal conductivity distribution (balanced brightness), while the higher P3ODT content reduced conductive regions, directly validating the observed electrical and thermoelectric behavior.

Hall effect tests were performed on P3ODT/P3OT/F$_4$-TCNQ doped films to quantify carrier mobility (μ) and carrier concentration (n). The results of these tests are shown in Table 1. Theoretically, the Seebeck coefficient was negatively correlated with the carrier concentration and positively correlated with the carrier mobility.[35,36] The conductivity (σ) was determined by the carrier mobility (μ) and the carrier concentration (n), and the relationship could be expressed as $\sigma = ne\mu$. Consistent with this framework, doped P3OT exhibited a high n value (1.79×10^{20} cm^{-3}), correlating with its elevated conductivity. As the P3ODT content increased, both n and σ decreased monotonically (Table 1), attributable to the bulky side chains of P3ODT sterically hindering F$_4$-TCNQ access to P3OT backbones, thereby suppressing conductive complex formation. However, a modest enhancement in carrier mobility was observed in blend films with an elevated proportion of P3ODT. This phenomenon was hypothesized as the wrapping of the

Table 1 Carrier mobility, carrier concentration and conductivity of blend-doped materials with different blending ratios

Sample	μ (cm^2 V^{-1} S^{-1})	n (cm^{-3})	σ (S cm^{-1})
Doped P3OT	1.41×10^{-1}	1.79×10^{20}	4.0348
Doped P3OT : P3ODT = 9 : 1	1.81×10^{-1}	1.35×10^{20}	3.9099
Doped P3OT : P3ODT = 7 : 3	38.2×10^{-1}	4.80×10^{18}	2.9366

branched alkyl side chains of P3ODT, which resulted in a smoother polymerization backbone. This finding offered further validation to the assertion that the reduction of grain boundary density in the AFM images (Fig. 4H–J) could enhance carrier mobility to a certain extent.

Conclusions

In this study, we synthesized viscoelastic conjugated polythiophene P3ODT featuring branched alkyl side chains and blended with linear-side-chain P3OT. The resulting blends were further doped with the molecular dopant F$_4$-TCNQ to fabricate flexible thermoelectric materials. Crucially, P3ODT incorporation mitigated film degradation by suppressing phase separation, yet simultaneously reduced conductive complex formation and crystallinity while increasing structural disorder. Although F$_4$-TCNQ effectively generated polarons/bipolarons in P3OT, its doping efficiency in P3ODT was limited due to steric hindrance from bulky side chains. Optimized thermoelectric performance emerged at P3ODT : P3OT = 1 : 9, achieving a peak power factor of 0.697 µW m^{-1} K^{-2}. This balance originated from the dual role of P3ODT: its alkyl side chains enhanced carrier mobility through backbone planarization, compensating for reduced carrier concentration and conductivity. Thus, blending of a second conjugated polymer with tailored side chains represents an effective strategy for enhancing thermoelectric properties in flexible organic materials, providing new molecular design principles for performance optimization.

Conflicts of interest

There are no conflicts to declare.

Data availability

Data for this article are available in the supplementary information (SI). Supplementary information is available. See DOI: https://doi.org/10.1039/d5lp00223k.

Acknowledgements

References

1 T. A. Yemata, Y. Zheng, A. Kyaw, X. Z. Wang, J. Song, W. S. Chin and J. W. Xu, *Front. Chem.*, 2020, **7**, 870.

2 J. S. Liang, J. Liu, P. F. Qiu, C. Ming, Z. Y. Zhou, Z. Q. Gao, K. P. Zhao, L. D. Chen and X. Shi, *Nat. Commun.*, 2023, **14**, 8442.

3 X. H. Chen, Z. Q. Gao, P. F. Qiu, W. W. Zheng, T. R. Wei, L. D. Chen and X. Shi, *Adv. Funct. Mater.*, 2025, **35**, 2501996.

4 Z. Fan, Y. Y. Zhang, L. J. Pan, J. Y. Ouyang and Q. Zhang, *Renewable Sustainable Energy Rev.*, 2021, **137**, 110448.

5 O. Bubnova, Z. U. Khan, A. Malti, S. Braun, M. Fahlman, M. Berggren and X. Crispin, *Nat. Mater.*, 2011, **10**, 429–433.

6 J. L. Bredas and G. B. Street, *Acc. Chem. Res.*, 1985, **18**, 309–315.

7 B. Tsuie, J. L. Reddinger, G. A. Sotzing, J. Soloducho, A. R. Katritzky and J. R. Reynolds, *J. Mater. Chem.*, 1999, **9**, 2189–2200.

8 S. Masoumi, S. O'Shaughnessy and A. Pakdel, *Nano Energy*, 2022, **92**, 106774.

9 S. H. Cho, J. W. Ha, C. E. Song, Y. H. Kang, M. J. Han, S. Lee and B. Park, *Chem. Eng. J.*, 2025, **508**, 160823.

10 X. L. Zhong, Y. L. Qiao, Q. J. Yin, Y. H. Wang and G. Zhou, *Compos. Interfaces*, 2025, **32**, 1033–1052.

11 A. Lis, K. Zazakowny, K. Wolski, S. Zapotoczny and K. T. Wojciechowski, *Chem. Eng. J.*, 2025, **515**, 163468.

12 Z. J. Chen, Y. Wen, Y. C. Xu, D. N. Li, Q. J. Le, S. Shin and J. Y. Ouyang, *Adv. Funct. Mater.*, 2025, **35**, 2424378.

13 D. L. Meyer, N. Schmidt-Meinzer, C. Matt, S. Rein, F. Lombeck, M. Sommer and T. Biskup, *J. Phys. Chem. C*, 2019, **123**, 20071–20083.

14 F. Zhong, Y. Y. Zheng, J. Song, L. D. Chen and H. Li, *Adv. Funct. Mater.*, 2025, 2507113.

15 H. Kim, S. B. Kim, S. Pyo, J. Jang and I. H. Jung, *Adv. Funct. Mater.*, 2025, **35**, 2422778.

16 A. Shinohara, C. J. Pan, Z. F. Guo, L. Y. Zhou, Z. H. Liu, L. Du, Z. C. Yan, F. J. Stadler, L. Wang and T. Nakanishi, *Angew. Chem., Int. Ed.*, 2019, **58**, 9581–9585.

17 Z. F. Guo, A. Shinohara, C. J. Pan, F. J. Stadler, Z. H. Liu, Z. C. Yan, J. L. Zhao, L. Wang and T. Nakanishi, *Mater. Horiz.*, 2020, **7**, 1421–1426.

18 T. J. Aubry, J. C. Axtell, V. M. Basile, K. J. Winchell, J. R. Lindemuth, T. M. Porter, J. Y. Liu, A. N. Alexandrova, C. P. Kubiak and S. H. Tolbert, *Adv. Mater.*, 2019, **31**, 1805641–1805647.

19 V. I. Arkhipov, P. Heremans, E. V. Emelianova, G. J. Adriaenssens and H. Bässler, *Appl. Phys. Lett.*, 2003, **82**, 3245–3247.

20 A. M. Glaudell, J. E. Cochran, S. N. Patel and M. L. Chabinyc, *Adv. Energy Mater.*, 2015, **5**, 1041072.

21 C. C. Wang, D. T. Duong, K. Vandewal, J. Rivnay and A. Salleo, *Phys. Rev. B:Condens. Matter Mater. Phys.*, 2015, **91**, 085205.

22 H. Méndez, G. Heimel, S. Winkler, J. Frisch, A. Opitz, K. Sauer, B. Wegner, M. Oehzelt, C. Röthel, S. Duhm, D. Többens, N. Koch and I. Salzmann, *Nat. Commun.*, 2015, **6**, 8560.

23 D. Kiefer, R. Kroon, A. I. Hofmann, H. D. Sun, X. J. Liu, A. Giovannitti, D. Stegerer, A. Cano, J. Hynynen, L. Y. Yu,

© 2025 The Author(s). Published by the Royal Society of Chemistry

RSC Appl. Polym., 2025, **3**, 1629–1636 | **1635**

Y. D. Zhang, D. Q. Nai, T. F. Harrelson, M. Sommer, A. J. Moulé, M. Kemerink, S. R. Marder, I. McCulloch, M. Fahlman, S. Fabiano and C. Muller, *Nat. Mater.*, 2019, **18**, 149.

24 D. T. Scholes, S. A. Hawks, P. Y. Yee, H. Wu, J. R. Lindemuth, S. H. Tolbert and B. J. Schwartz, *J. Phys. Chem. Lett.*, 2015, **6**, 4786–4793.

25 S. N. Patel, A. M. Glaudell, K. A. Peterson, E. M. Thomas, K. A. O'Hara, E. Lim and M. L. Chabinyc, *Sci. Adv.*, 2017, **3**, 1700434.

26 H. Martens, I. N. Hulea, I. Romijn, H. B. Brom, W. F. Pasveer and M. Michels, *Phys. Rev. B:Condens. Matter Mater. Phys.*, 2003, **67**, 121203.

27 G. Z. Zuo, X. J. Liu, M. Fahlman and M. Kemerink, *Adv. Funct. Mater.*, 2018, **28**, 1703280.

28 P. Pingel and D. Neher, *Phys. Rev. B:Condens. Matter Mater. Phys.*, 2013, **87**, 115209.

29 H. Hase, K. O'Neill, J. Frisch, A. Opitz, N. Koch and I. Salzmann, *J. Phys. Chem. C*, 2018, **122**, 25893–25899.

30 N. Saxena, J. Keilhofer, A. K. Maurya, G. Fortunato, J. Overbeck and P. Müller-Buschbaum, *ACS Appl. Energy Mater.*, 2018, **1**, 336–342.

31 Z. Fan, D. G. Du, H. Y. Yao and J. Y. Ouyang, *ACS Appl. Mater. Interfaces*, 2017, **9**, 11732–11738.

32 K. Kang, S. Watanabe, K. Broch, A. Sepe, A. Brown, I. Nasrallah, M. Nikolka, Z. P. Fei, M. Heeney, D. Matsumoto, K. Marumoto, H. Tanaka, S. Kuroda and H. Sirringhaus, *Nat. Mater.*, 2016, **15**, 896.

33 A. J. Tang, Y. P. Li, R. Wang, J. W. Yang, C. Q. Ma, Z. Li, Q. Zou and H. X. Li, *Chem. Commun.*, 2023, **59**, 1305–1308.

34 L. Ma, P. Hu, H. Jiang, C. Kloc, H. D. Sun, C. Soci, A. A. Voityuk, M. E. Michel-Beyerle and G. G. Gurzadyan, *Sci. Rep.*, 2016, **6**, 28510.

35 M. Ziati, N. Bekkioui and H. Ez-Zahraouy, *J. Phys. Chem. Solids*, 2022, **161**, 110409.

36 Y. Zhang, Q. Yang, C. Lin, R. J. Chen, S. R. Maliha, Y. Chen, J. J. Xu and C. J. Pan, *J. Mater. Chem. A*, 2024, **12**, 29262–29270.